

# Inductance Evaluation and Sensorless Control of a Concentrated Winding PM Vernier Machine

Tianjie Zou, *Student Member, IEEE*, Xun Han, Dong Jiang\*, *Senior Member, IEEE*,  
Ronghai Qu, *Fellow, IEEE*, and Dawei Li, *Member, IEEE*  
State Key Laboratory of Advanced Electromagnetic Engineering and Technology  
School of Electrical & Electronic Engineering  
Huazhong University of Science and Technology, Wuhan, 430074, China  
E-mail:jiangd@hust.edu.cn

**Abstract**—Due to the advantages of high torque density and simple mechanical structure, permanent magnet vernier (PMV) machines have attracted more and more research interests. In this paper, the inductance non-linearity of an advanced concentrated winding (CW) PMV machine is investigated with consideration of both magnetic saturation and cross coupling saturation under different  $d$ -axis and  $q$ -axis current loading. Then, the mathematical model with variable inductance matrix of the PMV machine is established through incorporation of finite element analysis (FEA) and surface fitting method. Further, a back-EMF based sensorless control method is developed for this PMV machine model with design of a current dependent state observer. Based on the sensorless algorithm, the influence of inductance variation on rotor position estimation performance is then quantitatively evaluated. Simulation results show that the PMV machine can be well controlled for steady and dynamic state operation, and the position estimation error is effectively decreased. Finally, the proposed sensorless control algorithm is validated through experimental tests of the PMV prototype machine.

**Index Terms**—Vernier permanent magnet machine, sensorless control, back-EMF, surface fitting, observer.

## I. INTRODUCTION

In recent years, permanent magnet vernier (PMV) machine is gaining much interest in direct drive applications due to its potential to overcome the bulkiness that most high power direct drive machines are subjected to. With superior torque density, compact mechanical structure, high reliability and inherent magnetic gear effect, PMV machines are promising alternatives in low speed, high torque applications such as wind power, electric propulsion and robotic servo system. In two decades since PMV machine was firstly presented in 1995 [1], researches about this kind of machine have been conducted on proposing novel topologies [2-7], establishing analytical theories [8-10] and modeling approaches [11-12], as well as comparison with commercial machines [13-14].

Despite the superiority in torque density, regular PMV machines with lap winding configuration tend to suffer from long end turns. To avoid this problem, concentrated windings were applied to PMV machines with special designed auxiliary tooth structure in the stator [15-17]. However, regular non-overlapping winding associated with such stator structure may be subjected to worse flux modulation effect and winding factor, which will result in torque reduction [18]. In [19], an advanced PMV machine with multiple working harmonics is proposed, which can improve the torque capability of non-

overlapping winding PMV machines.

So far, vector control algorithm is most commonly adopted for prototype test of PMV machines in literature, in which real time rotor position information through a position sensor is necessary. However, position sensors increase the cost, and degrade the reliability of the machine system. Therefore, it is desirable to incorporate sensorless control with PMV machines to further improve the overall reliability of the machine system. Generally, there are two strategies of sensorless control algorithms, i.e., high frequency injection methods suitable for slow speed or even standstill operation and back-EMF methods that work well at middle to high speeds [20].

The back-EMF based sensorless control method was firstly proposed only for surface mounted PM (SPM) machines with negligible spatial saliency. [21] developed an extended back-EMF method by building a unified mathematical model for both SPM and interior PM (IPM) machines, in which the rotor position information contained both in the back-EMF term and the saliency term can be accounted for. Among the back-EMF based sensorless algorithm, the model reference adaptive system (MRAS) observer is widely adopted. Due to the non-ideality of MRAS observer, the steady state position estimation error is usually inevitable, which may deteriorate the robustness and stability of the observer [22-24]. It has been reported in [24] that the inductance variation caused by magnetic saturation is a main source of position estimation error.

The influence of inductance nonlinearity caused by saturation and cross coupling saturation was discussed in [25-30]. [26] evaluated the inductance variation effects on position estimation error of SPM machines by proposing an “artificial inductance” concept. Through comparison of estimation error in control schemes with and without cross coupling saturation considered, [27] drew the conclusion that cross coupling saturation in regular SPM machines is negligible. Nevertheless, it is found that the presented machine illustrated in Fig. 1 exhibits obvious cross coupling saturation under considerable  $dq$ -axis current.

In this paper, the inductance characteristics of an advanced concentrated winding PMV (CW-PMV) machine is investigated. Based on the inductance analysis, a back-EMF based sensorless control algorithm is developed for this machine. The CW-PMV machine has been proposed, analyzed and prototyped in [19]. This control system is designed with

particular attention paid on non-linearity of the inductance matrix caused by saturation and cross coupling saturation. Through combination of FEA and surface fitting method, a current dependent inductance matrix is established. The non-linear inductance matrix is then substituted into the sensorless control algorithm to improve the position estimation capability. The machine structure and operation principle will be introduced in Section II. Section III will focus on developing the non-linear model of this machine through inductance evaluation. Then, Section IV will be devoted to design of the sensorless control algorithm. Finally, experimental validation of the prototype will be given in Section V.

## II. MACHINE STRUCTURE AND OPERATION PRINCIPLE

The exploded view of the CW-PMV machine is shown in Fig. 1. Briefly, the machine is constructed with a surface mounted rotor and a coil wound stator, with special designed auxiliary teeth to serve not only as flux path but also flux modulators. Due to the existence of auxiliary teeth, the number of stator slots for embedding windings and the number of flux modulators are decoupled. Then, the selection of the stator slot-pole combination becomes more flexible and non-overlapping windings can be applied. It should be noted that regular PMV machines are with uniformly distributed flux modulation poles (FMPs). While for the presented CW-PMV machine, there are different pitch angles between FMPs, as shown in Fig. 2. With this specially designed FMP disposition, additional working permeance as well as flux density harmonics are introduced, and higher torque capability can be achieved. The parameter  $k$  defined as the ratio of  $\theta$  to average slot pitch has been investigated in [19] and the optimal value is 1.3.

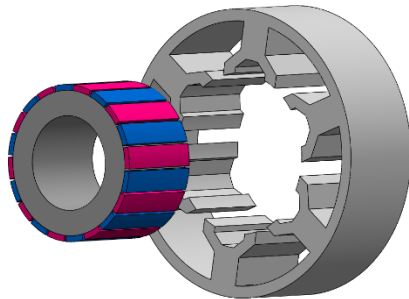


Fig. 1. Exploded view of the advanced CW-PMV machine.

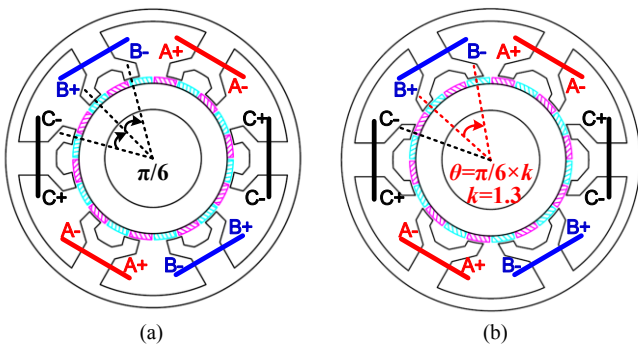


Fig. 2. Comparison of regular and the presented CW-PMV machine topology. (a) Regular PMV machine. (b) CW-PMV machine.

Generally, the number of auxiliary teeth  $Z$ , rotor pole pair

number  $P_R$  and stator pole pair number  $P_S$  of a PMV machine should satisfy the equation (1). For the CW-PMV machine,  $Z=12$ ,  $P_R=10$  and  $P_S=2$ . The stator MMF  $F_c$  due to the coil current can be expressed by (2), where  $t$  stands for the machine periodicity,  $N_s$  the turns in series per phase,  $I$  the rms value of phase current,  $k_{wv}$  the winding factor and  $\omega$  the electric velocity, respectively. For the CW-PMV machine, the fundamental pole pair number of the stator  $P_S=t=2$ .

$$Z = P_R \pm P_S \quad (1)$$

$$F_c(\theta_s, t) = \frac{3\sqrt{2}}{\pi t} N_s I \left[ \sum_{v=1,4,7,10,\dots} \frac{k_{wv}}{v} \cos(tv\theta_s - \omega t) \right] + \left[ \sum_{v=2,5,8,11,\dots} \frac{k_{wv}}{v} \cos(tv\theta_s + \omega t) \right] \quad (2)$$

$$\Lambda = \Lambda_0 + \sum_{i=1,2,3,\dots} \Lambda_{iZ} \cos(iZ\theta_s), \quad Z = \frac{P_f}{n_f} \quad (3)$$

It should be noted that only the armature magnetic field with pole pair number of  $P_R$  can be coupled with the PM rotor to produce steady torque. For a regular PM machine, the  $P_R^{\text{th}}$  armature field can only be produced through the interaction of the stator MMF harmonic with exactly the same pole number and the average airgap permeance. However, for the CW-PMV machine, the actually working permeance can be expressed as (3), where  $\Lambda_0$  and  $\Lambda_{iZ}$  are the constant component and amplitude of the permeance function harmonics, respectively.  $P_f$  stands for the total number of FMPs, and  $n_f$  is the number of neighboring FMPs connected to one main tooth. Accordingly, there are multiple working stator MMF harmonics, as shown in Fig. 3. The percentage of airgap flux density with the pole pair number of  $P_R$  contributed by these MMF harmonics, respectively, is given in Fig. 4.

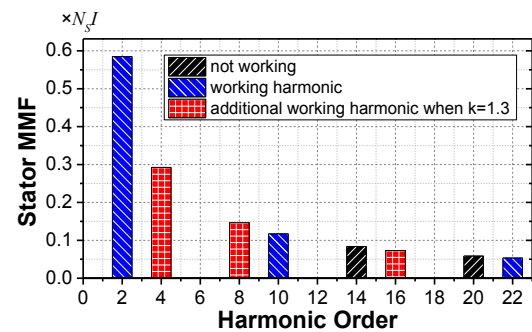


Fig. 3. Spectra of stator MMF harmonics.

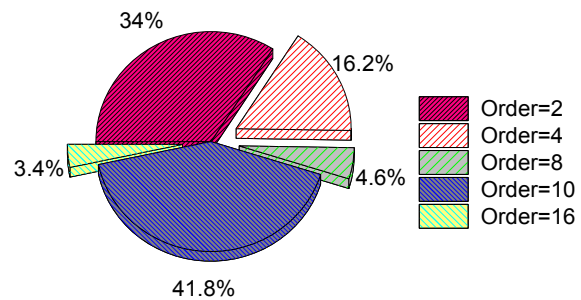


Fig. 4. Percentage of  $P_R^{\text{th}}$  flux density produced by stator working MMF harmonics.

### III. INDUCTANCE EVALUATION AND MODELLING

The winding inductance is an important parameter for the back-EMF based sensorless control algorithm, which is dependent on the stator pole number and the magnetic circuit design. Generally, the magnetic circuit of a PM machine is optimized by carefully choosing geometric parameters, which also relies on the stator pole number to a large extent. For regular PM machines, there exists only one working stator MMF harmonic that couples with the exciting magnetic field of rotor PMs. Thus, the pole number of the stator is easy to be determined. For PMV machines, the stator pole pair number is defined as lowest order of stator working MMF harmonic, which differs from the PM pole pair number.

From Section II, it can be seen that the CW-PMV machine with  $P_S=2$  operates with multiple working harmonics of stator MMF. Nevertheless, the 2<sup>nd</sup> order stator MMF harmonic contributes only 34%, while the 10<sup>th</sup> ( $P_R^{\text{th}}$ ) harmonic contributes nearly 42% of the whole stator working flux density. Therefore, the stator dimensions of this machine were designed according to the pole pair number of  $P_R$  to eliminate the margin of stator sizes such as yoke thickness and make full use of steel sheet material. In fact, the stator sizes of most PMV machines are designed according to the rotor instead of stator pole pair number, which may result in easier saturation and cross-coupling saturation than that of regular PM machines.

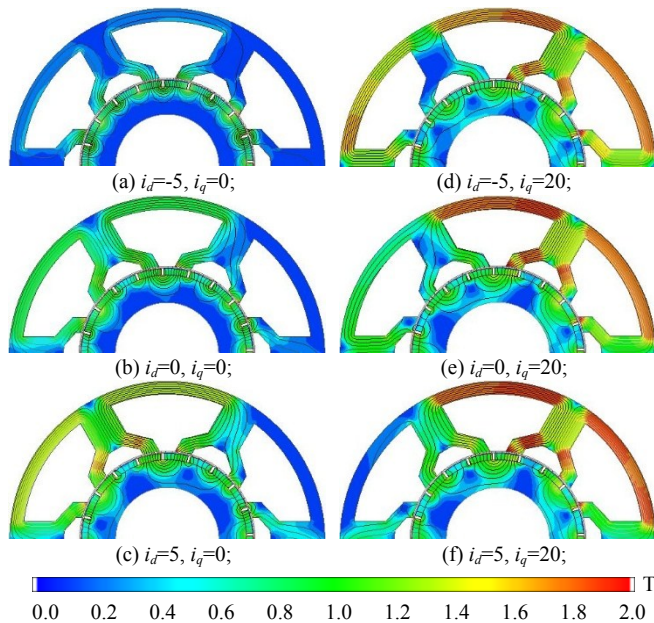


Fig. 5. Flux contour plots of the CW-PMV machine under different  $i_d$  and  $i_q$ .

Since the back-EMF based sensorless control algorithm is very sensitive to inductance variation, the influence of saturation and cross-coupling saturation on nonlinearity of the

$d$ -axis inductance  $L_d$  and  $q$ -axis inductance  $L_q$  should be evaluated. Fig. 5 illustrates the flux contour plots of the CW-PMV machine under different  $d$ -axis current  $i_d$  and  $q$ -axis current  $i_q$ . It can be seen that the flux density of the stator, especially the yoke part, changes a lot with  $i_d$  and  $i_q$ . As shown in Fig. 5(c), the stator tooth part under  $i_d=5A$  exhibits partial saturation, and the maximal flux density reaches  $\sim 1.6T$ . Moreover, when the machine operates on load condition with large value of  $i_q$ , the stator yoke gets into deep saturation with the flux density exceeding  $1.9T$ . In addition, the positive  $d$ -axis current together with  $i_q$  will further increase the saturation level, as illustrated in Fig 5(f). Since the yoke part is designed to be thinner than that of the regular counterparts with six-slot, four-pole combination, it is easily saturated under relatively large  $i_d$  and  $i_q$ . The deep saturation of stator yoke caused by either  $i_d$  or  $i_q$  will lead to variation of both  $L_d$  and  $L_q$ , since it provides path for both  $d$ - and  $q$ -axis magnetic circuit.

TABLE I  
MAIN PARAMETERS OF THE PROTOTYPE

Item	Value
Rated speed, rpm	300
Rated torque, Nm	21
Rated phase current, A	8.5
Rated phase voltage, V	86.6
Stator outer diameter, mm	122
Stator inner diameter, mm	68
Stack length, mm	85
Air-gap length, mm	0.8
PM thickness, mm	2.5
Turns in Series per Phase	214

In order to investigate the nonlinearity of inductance, several FEA cases with a set of  $i_d$  and  $i_q$  were built and the values of  $L_d$  and  $L_q$  under each case were calculated. The main design parameters of the FEA model are listed in Table I. Then, the surface fitting method were applied to approximate the quantitative expressions between  $L_d$ ,  $L_q$  and  $i_d$ ,  $i_q$ , according to their discrete values. Since the expressions of  $L_d$  and  $L_q$  will be used in the sensorless control program, the cubic polynomial fitting method were finally adopted to balance the fitting accuracy and computation resource consumption. Fig. 6 and Fig. 7 illustrate the comparison of  $L_d$  and  $L_q$  vs.  $i_d$  and  $i_q$ , both calculated through FEA and surface fitting method, respectively. The specific cubic polynomials of  $L_d(i_d, i_q)$  and  $L_q(i_d, i_q)$  are expressed in Eqn. (4) and (5), respectively. Moreover, The R-square value of  $L_d(i_d, i_q)$  and  $L_q(i_d, i_q)$  are 0.986 and 0.996, which are very close to 1. Meanwhile, the corresponding SSE (sum of squares due to error) values are  $3.78e^{-5}$  and  $9.68e^{-6}$ , which are approaching 0. Hence, the effectiveness of the fitting method is verified, and convincing inductance values can be obtained from the equations of  $L_d(i_d, i_q)$  and  $L_q(i_d, i_q)$ .

$$L_d(i_d, i_q) = [28.08, -0.2333, -0.1223, -0.0537, -0.0216, -0.0244, 5.244 \times 10^{-4}, 1.906 \times 10^{-3}, 8.749 \times 10^{-4}, 4.564 \times 10^{-4}] \cdot [1, i_d, i_q, i_d^2, i_d i_q, i_q^2, i_d^3, i_d^2 i_q, i_d i_q^2, i_q^3]^T \quad (4)$$

$$L_q(i_d, i_q) = [27.17, -0.0308, 0.2165, -0.0352, -0.0279, -0.0396, 1.518 \times 10^{-4}, 1.151 \times 10^{-3}, 8.722 \times 10^{-4}, 6.499 \times 10^{-4}] \cdot [1, i_d, i_q, i_d^2, i_d i_q, i_q^2, i_d^3, i_d^2 i_q, i_d i_q^2, i_q^3]^T \quad (5)$$



The whole back-EMF based sensorless control scheme is shown in Fig. 9. The control system is developed with typical modules of vector control algorithm, i.e., an outer speed controller loop and inner  $dq$ -axis current controller loop. In the simulation, the converter that drives the machine model is designed with 10 kHz switching frequency.

The mathematical model of the CW-PMV machine derived in Section III is presented as a state space expressed by Eqn. (11). It should be noted that although  $\hat{e}_d$  and  $\hat{e}_q$  are functions of  $dq$ -axis current, their differential values are negligible. **A**, **B** and **C** are matrices given in Eqn. (12). The input **u** and output  $\hat{\mathbf{y}}$  of the state space are  $dq$ -axis voltages and currents in the estimated reference frame, respectively.

$$\dot{\hat{\mathbf{x}}} = \mathbf{A} \cdot \hat{\mathbf{x}} + \mathbf{B} \mathbf{u}, \quad \hat{\mathbf{x}} = [\hat{i}_d, \hat{i}_q, \hat{e}_d, \hat{e}_q]^T, \quad \hat{\mathbf{y}} = \mathbf{C} \hat{\mathbf{x}} \quad (11)$$

An asymptotic state observer proposed in [31] is applied to calculate the estimated back-EMF, as illustrated in Fig. 10. The plant model describes the dynamics of the real machine, while the observer reconstructs the state variables of the machine in the estimated rotor reference. The state space equation of the observer is then written as (13), where  $\mathbf{y} = [i_{d\_mea}, i_{q\_mea}]$  and represents the measured currents in the estimated  $d$ - and  $q$ -axis rotor reference frame for state feedback. The matrix **L** is the feedback gain matrix that controls the estimation error of the state variable. It should be noted that **L** determines the dynamics of the observer, which should be carefully designed.

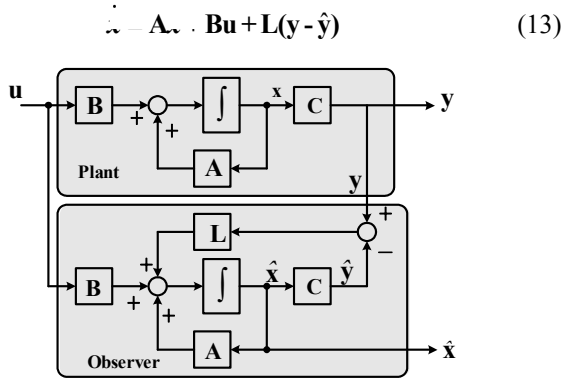


Fig. 10. Block diagram of observer.

The built asymptotic observer is a relatively complex 4<sup>th</sup> order system, and can be more easily analyzed by reasonable simplification. According to [31], the 4<sup>th</sup> observer can be regarded comprised of two orthogonal systems aligned with the  $d$ - and  $q$ -axis, respectively. Hence, the original system can be equalized to two 2<sup>nd</sup> order systems with equal dynamics. Consequently, the corresponding characteristic equation of the observer can be written as Eqn. (14), where  $\zeta_o$  and  $\omega_o$  represent the desired damping coefficient and natural frequency, respectively. By Combining Eqn. (11)-(14), the matrix **L** can be determined and expressed by Eqn. (15). Moreover, the stability of the observer can be verified by inspecting the pole assignment according to Eqn. (14). Practically,  $\zeta_o = 0.707$ , and  $\omega_o = 1200\pi$ . Hence, all the poles of the characteristic equation are located in the left-half plain, and the system is stable.

$$c(s) = \det(s\mathbf{I} - (\mathbf{A} - \mathbf{L}\mathbf{C})) = (s^2 + 2\zeta_o\omega_o s + \omega_o^2)^2 \quad (14)$$

$$\mathbf{L} = \begin{bmatrix} -\frac{r_s}{L_d(i_d, i_q)} + 2\zeta_o\omega_o & \frac{L_q(i_d, i_q)}{L_d(i_d, i_q)}\hat{\omega}_r \\ -\frac{L_q(i_d, i_q)}{L_d(i_d, i_q)}\hat{\omega}_r & -\frac{r_s}{L_d(i_d, i_q)} + 2\zeta_o\omega_o \\ \omega_o^2 L_d(i_d, i_q) & 0 \\ 0 & -\omega_o^2 L_d(i_d, i_q) \end{bmatrix} \quad (15)$$

The block diagram of the tracking controller is shown in Fig. 11. It can be seen that the estimated  $d$ -axis back-EMF component calculated from the observer in the estimated  $d$ - $q$  axis is substituted into the phase-locked loop (PLL) tracking controller, and forced to zero by the PI regulator. The speed and rotor position information acquired from the tracking are used to close the speed loop and achieve coordinate transformation, respectively.

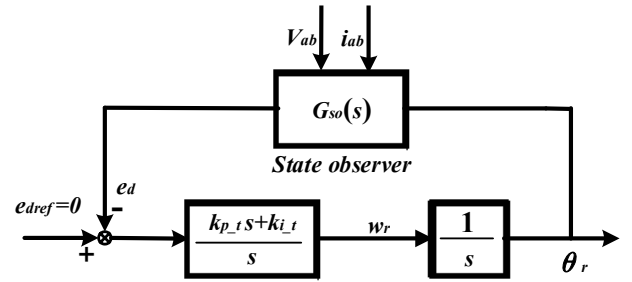


Fig. 11. Block diagram of the tracking controller.

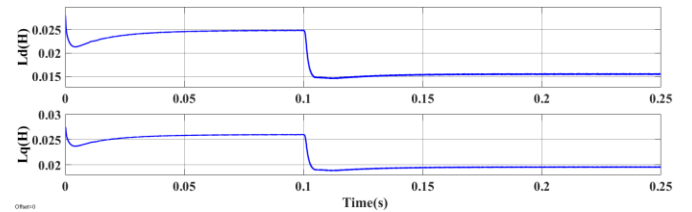


Fig. 12. Variation of  $L_d$  and  $L_q$  with no load start up and full load enabled at 0.1s.

Full simulation of the sensorless control algorithm has been conducted in Matlab/Simulink. Fig. 12 shows the variation of  $L_d$  and  $L_q$ , with no load start up and full load enabled at 0.1s. Since  $L_d$  and  $L_q$  changes significantly with the load torque, a constant inductance matrix used in the observer may lead to considerable position estimation error in the full load range.

Fig. 13 gives the results of estimated and real rotor position waveforms. In Fig. 13(a), the observer is constructed with constant inductance matrix obtained from FEA under open circuit condition, and more than 20 electrical degree position error occurs when full load is added. Nevertheless, when the variable inductance matrix is employed in the observer, the position estimation error is decreased to a great extent when load torque changes, which is illustrated in Fig. 13(b). Fig. 14 gives the position estimation error of the observer under different  $d$ - and  $q$ -axis current by adopting constant inductance matrix. It can be clearly seen that when the inductance nonlinearity is neglected in the sensorless algorithm, there will be considerable position estimation error, which will deteriorate the robustness and stability of the observer. Moreover, the overload capability may also be consequently weakened. Therefore, the effectiveness and necessity of the

proposed sensorless control method has been demonstrated by simulation.

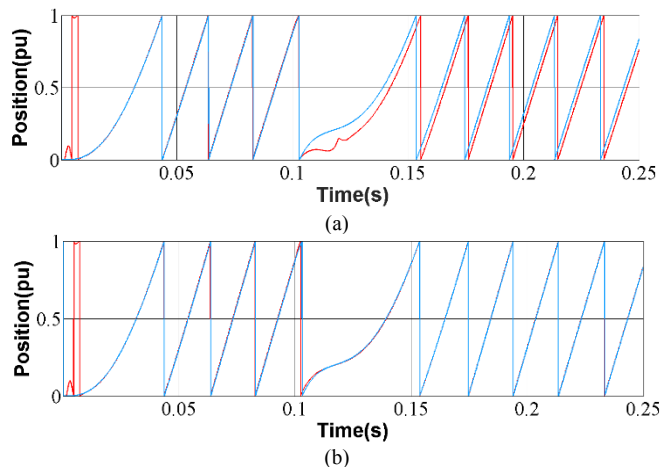


Fig. 13. Comparison of estimated and real rotor position, with full load enabled at 0.1s. (a) The observer is designed with constant inductance matrix. (b) The observer designed with variable inductance matrix.

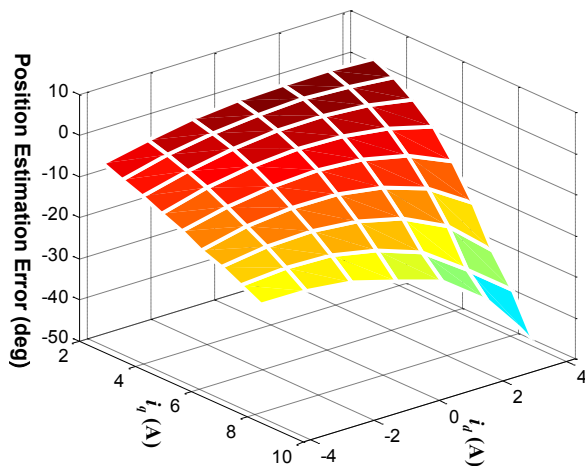


Fig. 14. Position estimation error of the observer under different  $d$ - and  $q$ -axis current by adopting constant inductance matrix.

## V. EXPERIMENTAL RESULTS

In order to validate previous analysis, a control system based on DSP of TMS320-F28335 is implemented for the CW-PMV machine prototype. It should be noted that the current dependent functions of  $L_d$  and  $L_q$  are adopted in the control program. The stator and rotor topology of the prototype are illustrated in Fig. 15, while the drive system and test bench are shown in Fig. 16. Under sensorless control, steady state waveforms of line current with 20Nm rated load torque and 300rpm rotating speed are shown in Fig. 17.

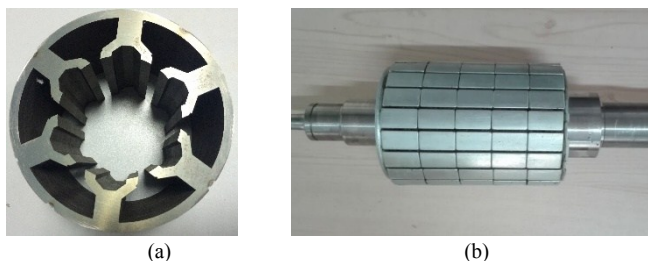


Fig. 15. Prototype of the CW-PMV machine. (a) Stator core. (b) Rotor.

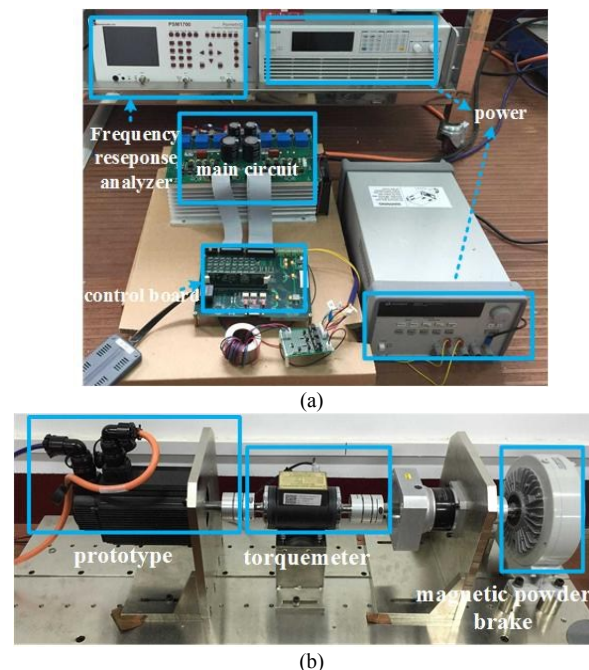


Fig. 16. Prototype and experimental implementation. (a) Drive system. (b) Test bench.

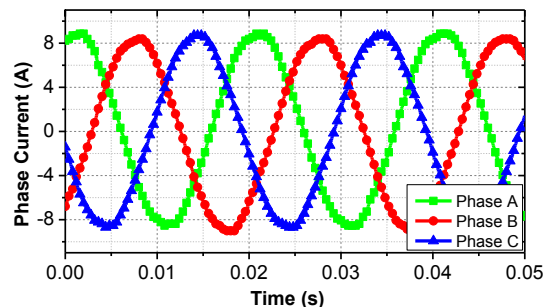


Fig. 17. Waveforms of line current under 20Nm load and 300 rpm.

A frequency response analyzer is utilized to test and verify the dynamics of each module in the sensorless control program. In order to investigate frequency response of the current loop, a small disturbance signal with smoothly varying frequency is added to the reference value of  $i_d$ . Then, the closed-loop Bode plot can be obtained by calculating the ratio of measured to input  $i_d$  disturbance. The open-loop Bode is further derived from the closed-loop one, which is given in Fig. 18. It can be seen that the gain crossover frequency is 185 Hz. Similarly, the open-loop Bode plots of the state observer and tracking controller are calculated and illustrated in Fig. 19 and Fig. 20, respectively. The bandwidth is  $\sim 500$  Hz for the observer and  $\sim 60$  Hz for the tracking controller.

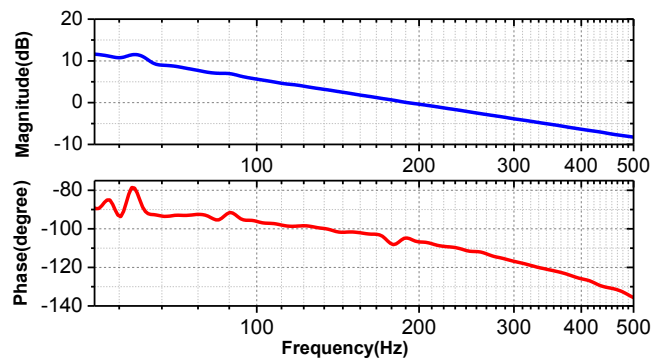


Fig. 18. Open-loop Bode plot of the current controller, derived from measured

closed-loop experimental results.

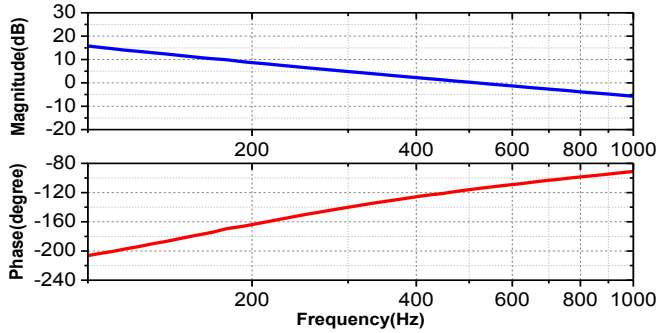


Fig. 19. Open-loop Bode plots of the observer, derived from measured closed-loop experimental results.

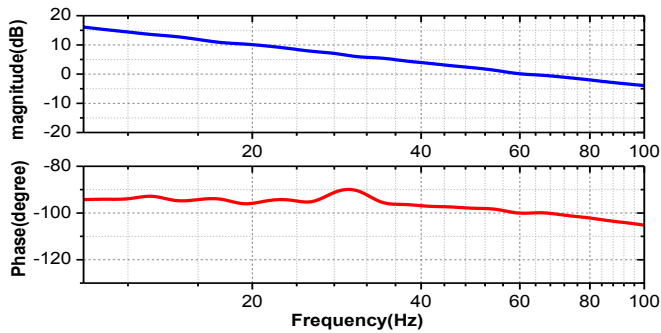


Fig. 20. Open-loop Bode plots of the tracking controller, derived from measured closed-loop experimental results.

Fig. 21 gives the dynamic process of estimated and actual speed curves under no load, variable speed operation. The prototype starts up and accelerates to 100 rpm in open-loop operation, and then switches to sensorless control. The machine keeps accelerating to 300rpm, and then slows down to 150rpm. It can be seen that the estimated speed has tracked well the real one. Fig. 22 shows the transient speed response to sudden change in load torque. It should be noted that the load torque provided by the magnetic powder brake cannot be enabled instantly. Hence, the dynamic speed drop at loading is not as much as its dynamic increase when the load is disabled. It can be seen that the developed sensorless algorithm works well under both variable speed and torque operation. The estimated and real rotor position at 300 rpm, 10Nm load are compared in Fig. 23. It can be seen that the estimated position tracks well with the actual one, and the position estimation error is low.

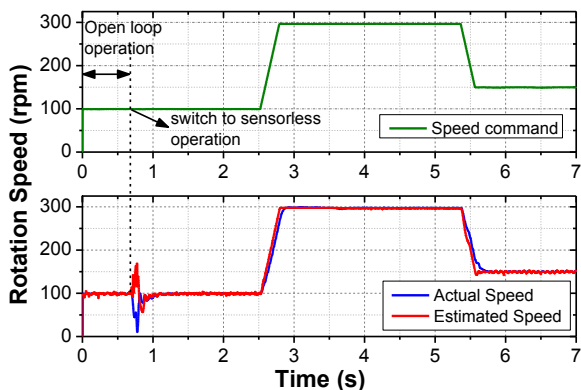


Fig. 21. Dynamic process of estimated and actual speed in variable speed operation.

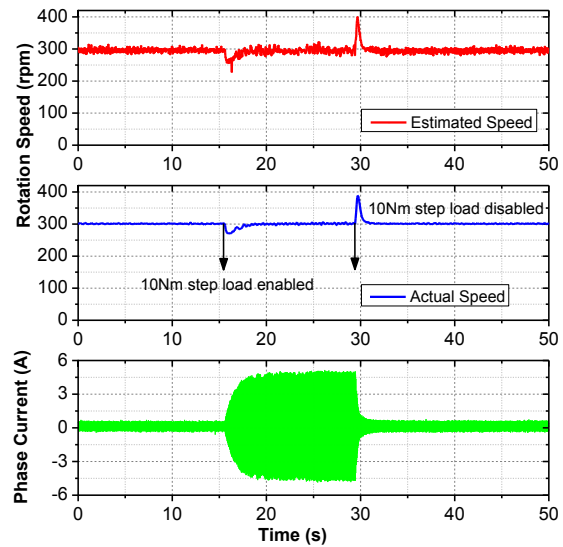


Fig. 22. Dynamic process of estimated and actual speed in step load operation.

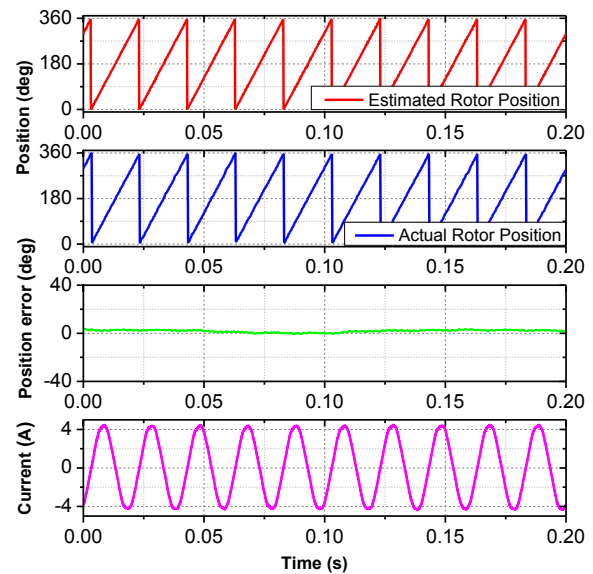


Fig. 23. Comparison of estimated and actual rotor position at 300 rpm, 10Nm.

In order to validate the effectiveness of the forgoing inductance evaluation and the proposed sensorless algorithm, the position estimation error, which is calculated as “rotor position obtained from the observer – rotor position obtained from the optical position encoder”, is investigated under different load condition. Fig. 24 gives the dynamic process of the position estimation error under sensorless control with constant inductance matrix in the observer. The constant inductance values are obtained from the no-load case. The load torque is slowly increased to clearly show the variation process of the estimated rotor position. It can be seen that the position error gradually increases along with the phase current. When the load torque reaches  $\sim 14.5$ Nm, the estimation error exceeds 30 elec. degree, and the system becomes unstable. To give an insight into the position error information under higher load, the machine is reloaded under sensed vector control, as shown in Fig. 25. It can be clearly seen that the transient position error in the observer gets to more than 40 degree. Hence, the load operation range is limited with constant inductance matrix implemented in the sensorless algorithm.

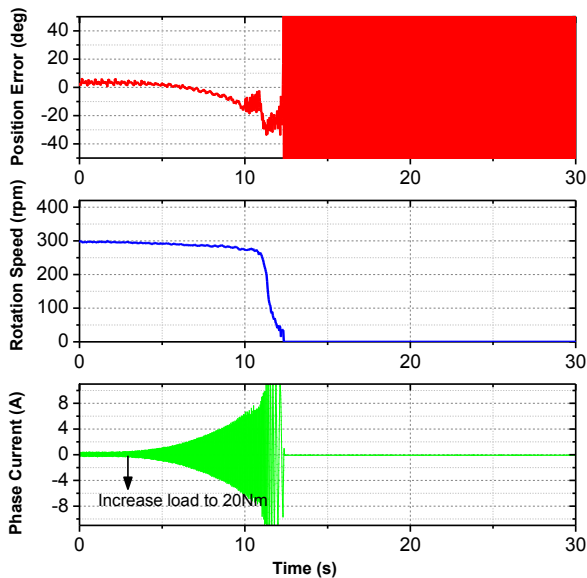


Fig. 24. Dynamic process the position error with constant inductance matrix implemented in the sensorless program.

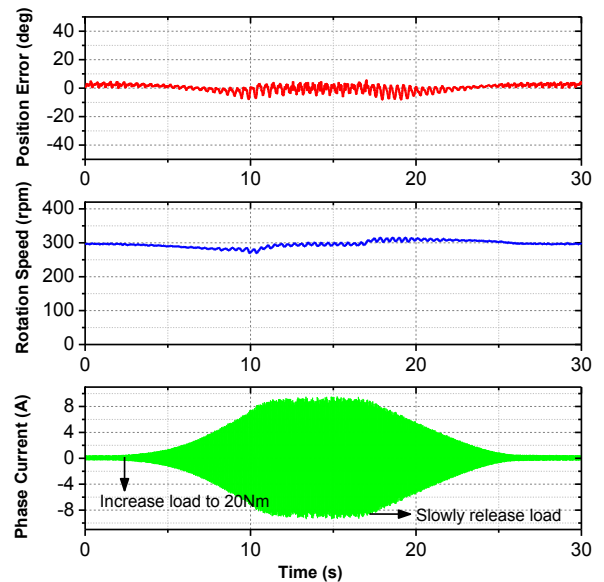


Fig. 26. Dynamic process the position error with current dependent inductance matrix implemented in the sensorless program.

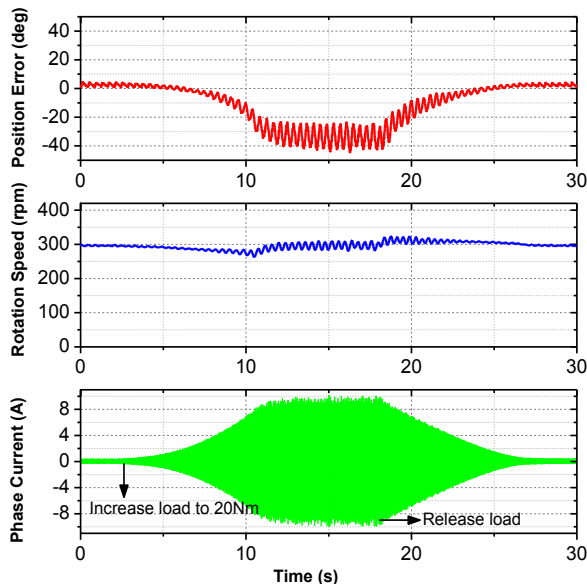


Fig. 25. Dynamic process the position error with constant inductance matrix implemented under sensed vector control.

Fig. 26 gives the position estimation error information under the proposed sensorless algorithm with current dependent inductance matrix in the back-EMF observer. It can be clearly seen that the position estimation error is significantly decreased. Moreover, the load operation range is extended. Hence, the effectiveness of the proposed sensorless control algorithm is validated. It should be noted that although the inductance non-linearity is the main focus of this paper, the accuracy of the stator resistance is also influential in the back-EMF estimation at low speed operation. Nevertheless, in the variable load tests above with the rated speed of 300rpm, the back-EMF is dominated by the term  $\omega_r \psi_m$ , and the influence of resistance variation due to winding temperature drift can be neglected.

## VI. CONCLUSION

Due to the advantages of high torque density and compact mechanical structure, permanent magnet vernier (PMV) machine has become a promising alternative in direct-drive application, and keeps gaining increasing research interests. This paper gives a study on modeling and sensorless control of an advanced concentrated winding PMV (CW-PMV) machine, with particular attention paid on the inductance non-linearity.

Through investigation of the current excited magnetic field, it has been found that the characteristics of multiple working MMF harmonics for PMV machines may result in easier magnetic saturation and cross coupling saturation than that of regular PM machines, which has been verified by inductance evaluation. Since neglecting of inductance variation may result in considerable position estimation error in sensorless operation, a mathematical model of the CW-PMV machine with current dependent inductance matrix has been built in  $dq$ -axis reference frame. The variable inductance function of both  $d$ - and  $q$ - axis current is established by incorporating FEA and the surface fitting method.

Based on the non-linear model, a back-EMF observer based sensorless vector control algorithm has been developed. The current controller, speed controller, observer and PLL tracking controller have been designed and simulated for the PMV machine drive in Matlab/Simulink. To validate the analysis results, a sensorless control system for the PMV machine prototype has been implemented. Experimental evaluation from no load to full load sensorless operation has been conducted. Test results not only have shown good control performance under start-up, speed change and load change process, but also have verified the effectiveness of the sensorless algorithm on reducing position estimation error.

## ACKNOWLEDGMENT

This work was supported by National Natural Science Foundation of China (NSFC) under Project No. 51337004.

## REFERENCES

- [1] A. Ishizaki, et al., "Theory and optimum design of PM vernier motor," in *Proc. IEE Int. Conf. Electrical Machines and Drives '95*, 1995, pp. 208–212.
- [2] A. Toba and T. Lipo, "Novel dual-excitation permanent magnet vernier machine," in *Conf. Rec. 34th IEEE IAS Annu. Meeting*, Oct. 1999, vol. 4, pp. 2539-2544.
- [3] S. Niu, S. L. Ho, W. Fu, and L. Wang, "Quantitative comparison of novel vernier permanent magnet machines," *IEEE Trans. Magn.*, vol. 46, no. 6, pp. 2032–2035, Jun. 2005.
- [4] D. Li, R. Qu, J. Li, and W. Xu, "Consequent pole, toroidal winding, outer rotor vernier permanent magnet machines," *IEEE Trans. Ind. Appl.*, vol. 51, no. 6, pp. 4470-4481, Nov./Dec. 2015.
- [5] F. Zhao, T. Lipo, B. Kwon, "A novel dual-stator axial-flux spoke-type permanent magnet Vernier machine for direct-drive applications," *IEEE Trans. Magn.*, vol. 50, no. 11, pp. 8104304, Nov. 2014.
- [6] T. Zou, D. Li, R. Qu, J. Li and D. Jiang, "Analysis of a dual-rotor, toroidal-winding, axial-flux vernier permanent magnet machine," *IEEE Trans. Ind. Appl.*, accepted.
- [7] D. Li, R. Qu, and T. Lipo, "High power factor vernier permanent magnet machines," *IEEE Trans. Ind. Appl.*, vol. 50, no. 6, pp. 3664-3674, Nov./Dec. 2014.
- [8] B. Kim, and T. Lipo, "Operation and design principles of a PM vernier motor," *IEEE Trans. Ind. Appl.*, vol. 50, no. 6, pp. 3656-3663, Nov./Dec. 2014.
- [9] D. Li, R. Qu, J. Li, L. Wu and W. Xu, "Analysis of torque capability and quality in vernier permanent magnet machines," *IEEE Trans. Ind. Appl.*, vol. 52, no. 1, pp. 125-135.
- [10] L. Wu, R. Qu, D. Li, and Y. Gao, "Influence of pole ratio and winding pole numbers on performances and optimal design parameters of surface permanent-magnet vernier machines," *IEEE Trans. Ind. Appl.*, vol. 51, no. 5, pp. 3707-3715, Sept./Oct. 2015.
- [11] L. Jian, G. Xu, C. C. Mi, K. T. Chau and C. C. Chan, "Analytical method for magnetic field calculation in a low-Speed permanent-magnet harmonic machine," *IEEE Trans. Energ. Convers.*, vol. 26, no. 3, pp. 862-870, Sept. 2011.
- [12] G. Liu, S. Jiang, W. Zhao and Q. Chen, "A new modeling approach for permanent magnet vernier machine with modulation effect consideration," *IEEE Trans. Magn.*, vol. 53, no. 1, pp. 1-12, Jan. 2017.
- [13] S. Gerber, R. Wang, "Design and evaluation of a PM vernier machine," in *Proc. 2015 IEEE Ener. Con. Cong. & Exp.*, Sep. 2015, pp.5188- 5194.
- [14] B. Kim, T. Lipo, "Design of a surface PM vernier motor for a practical variable application," in *Proc. 2015 IEEE Ener. Con. Cong. & Exp.*, Sep. 2015, pp.776- 783.
- [15] K. Okada, N. Niguchi, and K. Hirata, "Analysis of a vernier motor with concentrated windings," *IEEE Trans. Magn.*, vol. 49, no. 5, pp. 2241–2244, May 2013.
- [16] J. Yang, G. Liu, W. Zhao, Q. Chen, Y. Jiang, L. Sun, and X. Zhu, "Quantitative comparison for fractional-slot concentrated-winding configurations of permanent-magnet vernier machines," *IEEE Trans. Magn.*, vol. 49, no. 7, pp. 3826–3829, Jul. 2013.
- [17] L. Xu, G. Liu, W. Zhao, J. Ji, H. Zhou, W. Zhao and T. Jiang, "Quantitative comparison of integral and fractional slot permanent magnet vernier motors," *IEEE Trans. Energy Convers.*, vol. 30, no. 4, pp. 1483–1495, Dec. 2015.
- [18] Xu, G., L. Jian, W. Gong, and W. Zhao, "Quantitative comparison of flux-modulated interior permanent magnet machines with distributed windings and concentrated windings," *Progress In Electromagnetics Research*, vol. 129, 109-123, 2012.
- [19] T. Zou, D. Li, R. Qu, D. Jiang and J. Li, "Advanced high torque density PM vernier machine with multi working harmonics," *IEEE Trans. Ind. Appl.*, accepted.
- [20] S. Jurkovic, E. G. Strangas, "Design and analysis of a high-gain observer for the operation of SPM machines under saturation," *IEEE Trans. Energ. Convers.*, vol. 26, no. 2, pp. 417-427, June. 2011.
- [21] Z. Chen, M. Tomita, S. Doki, and S. Okuma, "An extended electromotive force model for sensorless control of interior permanent-magnet synchronous motors", *IEEE Trans. Ind. Electron.*, vol. 50, no. 2, pp. 288–295, Apr. 2003.
- [22] B. Nahid-Mobarakeh, F. Meibody-Tabar and F. M. Sargos, "Back EMF Estimation-Based Sensorless Control of PMSM: Robustness With Respect to Measurement Errors and Inverter Irregularities," *IEEE Trans. Ind. Appl.*, vol. 43, no. 2, pp. 485-494, Mar/Apr, 2007.
- [23] J. Holtz, "Acquisition of Position Error and Magnet Polarity for Sensorless Control of PM Synchronous Machines," *IEEE Trans. Ind. Appl.*, vol. 44, no. 4, pp. 1172-1180, July/Aug. 2008.
- [24] S. Bolognani, S. Calligaro and R. Petrella, "Design Issues and Estimation Errors Analysis of Back-EMF-Based Position and Speed Observer for SPM Synchronous Motors," *IEEE Journal of Emerging and Selected Topics in Power Electronics*, vol. 2, no. 2, pp. 159-170, June, 2014.
- [25] B. Stumberger, G. Stumberger, D. Dolinar, A. Hamler, and M. Trlep, "Evaluation of saturation and cross-magnetization effects in interior permanent-magnet synchronous motor," *IEEE Trans. Ind. Appl.*, vol. 39, no. 5, pp. 1264–1271, Sep. 2003.
- [26] K. Lu, X. Lei, and F. Blaabjerg, "Artificial Inductance Concept to Compensate Nonlinear Inductance Effects in the Back EMF-Based Sensorless Control Method for PMSM," *IEEE Trans. Energ. Convers.*, vol. 28, no. 3, pp. 593-600, Sept. 2013.
- [27] Z. Q. Zhu, Y. Li, D. Howe, C. M. Bingham, and D. Stone, "Influence of machine topology and cross-coupling magnetic saturation on rotor position estimation accuracy in extended back-EMF based sensorless PM brushless AC drives," In *Proc. 42nd IAS Annu. Meet.*, 2007, pp. 2378-2385.
- [28] P. Sergeant, F. De Belie and J. Melkebeek, "Effect of Rotor Geometry and Magnetic Saturation in Sensorless Control of PM Synchronous Machines," *IEEE Trans. Magn.*, vol. 45, no. 3, pp. 1756-1759, March 2009.
- [29] S. Ichikawa, M. Tomita, S. Doki and S. Okuma, "Sensorless Control of Synchronous Reluctance Motors Based on Extended EMF Models Considering Magnetic Saturation With Online Parameter Identification," *IEEE Trans. Ind. Appl.*, vol. 42, no. 5, pp. 1264-1274, Sept.-Oct. 2006.
- [30] T. Zou, X. Han, D. Jiang, R. Qu and D. Li, "Modeling and sensorless control of an advanced concentrated winding vernier PM machine," *2016 XXII International Conference on Electrical Machines (ICEM)*, Lausanne, 2016, pp. 1112-1118.
- [31] P. Kshirsagar, R. P. Burgos, J. Jang, A. Lidozzi, F. Wang, D. Boroyevich, and S. Sul, "Implementation and Sensorless Vector-Control Design and Tuning Strategy for SMPM Machines in Fan-Type Applications," in *IEEE Trans. Ind. Appl.*, vol.48, no.6, pp.2402-2413, Nov.-Dec. 2012.